Soft Matter

Accepted Manuscript

This is an *Accepted Manuscript*, which has been through the Royal Society of Chemistry peer review process and has been accepted for publication.

Accepted Manuscripts are published online shortly after acceptance, before technical editing, formatting and proof reading. Using this free service, authors can make their results available to the community, in citable form, before we publish the edited article. We will replace this *Accepted Manuscript* with the edited and formatted *Advance Article* as soon as it is available.

You can find more information about *Accepted Manuscripts* in the Information for Authors.

Please note that technical editing may introduce minor changes to the text and/or graphics, which may alter content. The journal's standard Terms & Conditions and the Ethical guidelines still apply. In no event shall the Royal Society of Chemistry be held responsible for any errors or omissions in this *Accepted Manuscript* or any consequences arising from the use of any information it contains.

ROYAL SOCIETY OF CHEMISTRY

www.rsc.org/softmatter

Mesoscale aggregation properties of C_{60} in toluene and chlorobenzene†

Rong-Hao Guo,[a] Chi-Chung Hua,*[,a] Po-Chang Lin,[b] Ting-Yu Wang,[c] and Show-An Chen[d]

[a] Department of Chemical Engineering, National Chung Cheng University, Chiayi 621, Taiwan.

[b] National Synchrotron Radiation Research Center, Hsinchu 300, Taiwan.

[c] Instrumentation Center, National Taiwan University, Taipei 106, Taiwan.

[d] Department of Chemical Engineering, National Tsing Hua University, Hsinchu 300, Taiwan.

Mesoscale aggregation properties of C_{60} in two distinct aromatic solvents (toluene and chlorobenzene) and a practical range of concentrations (c=1-2 and c=1-5 mg/mL, respectively) were systematically explored by static/dynamic light scattering (SLS/DLS), small angle X-ray scattering (SAXS), depolarized dynamic light scattering (DDLS), and cryogenic transmission electron microscopy (cryo-TEM) analyses. The central observations were as follows: (1) Aggregate species of sizes in the range of several hundred nanometers have been independently revealed by SLS, DLS, and DDLS analyses for both solvent systems. (2) DDLS and cryo-TEM

* Corresponding author. E-mail: chmcch@ccu.edu.tw

† Electronic supplementary information (ESI) available: Detailed information about the UV-vis absorption spectra of fullerene solutions, effects of laser-light exposure time and sonication time on fullerene solution dynamics, SALS intensity profiles of two fullerene sample solutions, evaluation of the radius of cylindrical aggregates, estimation of number density of C_{60} clusters, estimation of confinement tube diameter, and OM/SEM images and XRD patterns of drop-casting thin films.

features further revealed that while C_{60} clusters are notably anisotropic (rod-like) in chlorobenzene, they are basically isotropic (spherical) in toluene. (3) Detailed analyses of combined SLS and SAXS profiles suggested that varied, yet self-similar, solvent-induced aggregate units were responsible for the distinct (mesoscale) aggregation features noted above. (4) From a dynamic perspective, specially commissioned DLS measurements ubiquitously displayed two relaxation modes (fast- and slow-mode), with the second (slow) mode being *q* (wave vector) independent. While the fast mode in both solvent systems was basically diffusive by nature and leads to geometrical features in good agreement with the static analyses above, the slow mode was analyzed and tentatively suggested to reflect the effect of mutual confinement. (5) Micron-scale aggregate morphology of drop-casting thin films displays similarly contrasting features for the two solvent media used. Overall, this study suggests that solvent-induced, nanoscale, aggregate units may be a promising factor to control a hierarchy of microscopic aggregation properties of C_{60} solutions and thin films.

1. Introduction

Making use of the self-organization phenomena of fullerene and its derivatives in solution state to fabricate tunable nanoscale/mesoscale morphologies in thin films remains an attractive goal for current applications with field effect transistors,[1] photovoltaics,[2,3] and biomedicines.[4] Previous research had unveiled a number of solution-processed schemes to control the morphological features of various fullerene species through liquid-liquid interfacial precipitation,[5,6] template assisted dip drying,[7] solvent-induced self-assembly method,[8,9] and drop drying process.[5,10-13] Aqueous colloidal dispersions of fullerene aggregate can also be produced through solvent exchange process or extended mixing in water.[14-16] The success of these schemes, invariably, must rely on good knowledge about the aggregation properties in the solvent medium and processing scheme utilized, as reflected in the recent findings outlined below.

Light scattering analyses had previously revealed that fullerenes in a variety of organic solvent media including benzene,[17,18] toluene,[19] and mixed-solvent solutions[20-22] ubiquitously produce aggregate clusters of several hundred nanometers in size, many with clearly defined fractal structure within otherwise isotropic clusters. Combined dynamic light scattering and UV-vis spectroscopy analyses led to similar observation regarding the mean aggregate size of C_{60} in benzonitrile solutions.[23] In practice, the aggregation properties of C_{60} solutions can be affected by a handful of experimental or preparatory factors—often judged posterior through

the thin-film morphologies cast from different fullerene solutions—such as fullerene concentration,[24-26] pre-treatments with sonication or intense stirring,[27,28] polarity of the solvent species,[22,29-32] functional groups tethered on the fullerene,[26,33,34] and, in particular, the specific solvents utilized to dissolve fullerenes.[11-13] Clearly, the detailed interplay in these processes is of critical importance to understand in order to tailor the self-organization phenomena of fullerene for a wide range of current and emerging nanotechnological applications.[12,35]

Despite these generic features known to date, there have been few studies dedicated to revealing the multiscale structural features of C_{60} aggregates under conditions of varying solvent medium or fullerene concentration, two of the most commonplace experimental variables. In this study, static/dynamic light scattering (SLS/DLS), depolarized dynamic light scattering (DDLS), small-angle X-ray scattering (SAXS), and cryogenic transmission electron microscopy (cryo-TEM) measurements were employed to systematically explore the aggregation properties of C_{60} in two distinct solvent media (i.e., toluene and chlorobenzene) and a range of concentrations (i.e., c=1-2 and c=1-5 mg/mL, respectively). Revealing fullerene aggregation properties in these two organic solvent media has been motivated in part by an imperative need to control the mesoscale aggregation features in polymer/fullerene hybrid solution and thin film for the fast growing applications with organic solar cells, where utilization of either solvent had been noted to result in distinct device performances.[36] Computer simulations of late further revealed the detailed mechanisms these two solvent media

individually impact the solvation and aggregation behaviors of two standard fullerene species, i.e., C_{60}[37]and PCBM (phenyl-C_{61}-butyric-acid methyl ester).[38]

Combined DDLS feature and cryo-TEM imaging first identified that while C_{60} aggregate clusters are notably anisotropic in shape in chlorobenzene, they are basically isotropic in toluene, with a mean size of several hundred nanometers for all sample solutions investigated. SAXS analysis further revealed that these clusters are bolstered by distinct, solvent-induced, nanoscale aggregate units, which appear to organize themselves into self-similar, mesoscale (fractal) clusters as implied by a detailed analysis of combined SLS and SAXS profiles. The overall features were in accord with the scanning electron microscopy (SEM) morphologies of drop-casting thin films of C_{60} that were clearly indicative of the impact of the solvent medium employed. Finally, DLS features revealing peculiar relaxation behavior in both C_{60} solvent systems are discussed in conjunction with the static features above.

This paper is organized as follows: we first describe the materials, sample preparations, experimental procedures, and analyzing schemes. Afterward, the bulk features of fullerene aggregates in two different solvent media are characterized using DDLS and cryo-TEM schemes, while the building aggregate units and the mesoscale fractal structures are analyzed using a combination of SLS and SAXS profiles. As had rarely been done, the dynamic features of C_{60} solutions were scrutinized using specially commissioned DLS protocol, and the peculiarities so unveiled are discussed in conjunction with the static features above and

tentatively interpreted in the context of confinement effects. Finally, we summarize this work with some future outlooks.

2. Experimental

2.1 Materials and sample preparations

Buckminsterfullerene (C_{60}) of 98% purity (Aldrich Chemical) was used as received without further purification. The solvent used to dissolve fullerene, chlorobenzene (Aldrich Chemical, ≥99.5 % purity) or toluene (Mallinckrodt Chemical, ≥99.5 % purity), was filtered through a 0.22 μm PVDF filter (Millipore Millex-GN) to remove dusts. The sample vials were washed with detergent and then treated with filtered deionized (DI) water. Sample solutions of C_{60} with a range of concentrations (c=1-2 and c=1-5 mg/mL for toluene and chlorobenzene, respectively) were prepared with the filtered solvent. The sample solutions were sonicated 10 h per day at 50 °C with the aid of an external water circulation system for 4 days and stored in dark, autodry box at room temperature to avoid fullerene oxidation and aggregates so induced.[19,39] Note that the ranges of concentrations presently investigated all fall below the known maximum solubility of C_{60}, which was reported to be about 5 mg/mL for chlorobenzene and 2 mg/mL for toluene at 50 °C.[40,41] Besides, sonication was found to expedite the dissolution process during sample preparation, although it had been suggested that this treatment could inevitably aid the formation of large fullerene clusters.[28,42] In light scattering experiments, each sample solution

was further filtered into dust-free vial using 0.45 μm PVDF filter and then kept stationary for 12 h before use. All light scattering measurements were conducted at 25±0.1 °C.

It should be mentioned that the strategies of sample preparation described above were also meant to facilitate future applications with conjugated polymer/fullerene hybrid solution systems, where elevated system temperature and long-term sonication seem necessary to facilitate the experiment.[43,44] In this case, it is of interest to explore the underlying fullerene (molecular vs. colloidal) state[28] which, as we show herein, was dominated by (stabilized) colloidal aggregates along with a certain fraction of molecularly dispersed C_{60} on the experimental timescale. Nevertheless, effects of laser-light exposure time and sonication time of the sample solutions have been scrutinized, as shown in Fig. S2 of ESI. The results shed light on the relative stability of C_{60} aggregates formed in two different solvent media.

2.2 Static/Dynamic light scattering (SLS/DLS)

Light scattering measurements were performed on a laboratory-built apparatus as described elsewhere.[45] The instrument was equipped with a photon counting photomultiplier tube (Hamamatsu, H10682-01) linked to a counting board (Hamamatsu, M9300). Note, however, that a 80 mW diode laser (Power Technology, λ_0 = 785 nm) was used instead as the incident light to avoid absorptions of C_{60} in the visible-light region, especially at relatively high concentrations.[17,20] UV-vis spectrometer was utilized to confirm that C_{60} has negligible

absorption at the incident light wavelength (see Fig. S1, ESI). As indicated by the results shown in Fig. S2 of ESI, however, long laser-light exposure time may result in some appreciable change of the aggregation state, especially for C_{60}/toluene solutions. To minimize its effect, each individual light scattering measurement was finished within 3 h. The incident laser beam was vertically polarized with respect to the light scattering plane, and was later focused on the cylindrical scattering cell with an inner diameter of 2.1 cm (Hellma, 540.115) equipped with a screwed cap and peltier thermal controller which maintains the measuring temperature to within 25±0.1 °C.

In the SLS experiment, the q dependence of the excess scattering intensity, described by the relation $I_{ex}(q)=\left[I_{solu}(q)-I_{solv}(q)\right]/I_{tol}(q)$, is investigated, where I_{solu} and I_{solv} denote the time-averaged scattering intensities of the solution and the solvent, respectively, and I_{tol} is the average scattering intensity of toluene measured in the same apparatus; q represents the scattering vector and is defined as $q=(4\pi n/\lambda_0)\sin(\theta/2)$, with n, λ_0 and θ being solvent refractive index, the wavelength of the incident light in vacuum, and the scattering angle, respectively. Measurements were conducted in a range of scattering angles $\theta = 30° - 140°$.

In the DLS experiment, the normalized intensity autocorrelation function, $g^{(2)}(q,t)$, was collected in a homodyne mode, which can be related to the normalized field autocorrelation function, $\left|g^{(1)}(q,t)\right|$, through the Siegert relation:[46] $g^{(2)}(q,t)=1+\beta\left|g^{(1)}(q,t)\right|^2$, where β ($0 < \beta < 1$) is the spatial coherence factor depending on the detection optics. In the case of multiple

relaxation processes, $\left|g^{(1)}(q,t)\right|$ can be expressed in terms of the relaxation time distribution function, $A(\tau)$, as

$$\left|g^{(1)}(q,t)\right| = \int_0^\infty A(\tau)\exp(-t/\tau)\mathrm{d}\tau \qquad (1)$$

where $A(\tau)$ represents the intensity-weighted contribution associated with the relaxation time constant τ. The detailed distribution may be obtained by Laplace inversion, and the individual modes are often retrieved from the commercial software CONTIN.[47] The average relaxation time of each individual mode can be evaluated by the relation $\langle\tau_i\rangle = \sum_n A_n(\tau)\tau_n / \sum_n A_n(\tau)$, where index n sums the entire regime that has been assinged to the i^{th} mode. To analyze the relaxation mechanism, the average decay rate $\langle\Gamma_i\rangle$ can be defined as $\langle\Gamma_i\rangle = 1/\langle\tau_i\rangle$, and its q dependence may be expressed by $\langle\Gamma_i\rangle \sim q^\alpha$, e.g., α=2 for diffusive motions.

For any diffusive mode, $\langle\Gamma\rangle_\mathrm{d}$, as revealed in the analysis above, cumulant expansion can be further employed to find the mean size and its polydispersity:[48]

$$\ln\left|g^{(1)}(t)\right| = -\langle\Gamma\rangle_\mathrm{d} t + \frac{\mu_2}{2!}t^2 - \frac{\mu_3}{3!}t^3 + \ldots \qquad (2)$$

where $\langle\Gamma\rangle_\mathrm{d}$ is the average decay rate and may be expressed by $\langle\Gamma\rangle_\mathrm{d} = \int_0^\infty \Gamma_\mathrm{d} G(\Gamma_\mathrm{d})\mathrm{d}\Gamma_\mathrm{d}$, and μ_i represents the i^{th} moment of the decay rate distribution function, $G(\Gamma_\mathrm{d})$: $\mu_i = \int_0^\infty \left(\Gamma_\mathrm{d} - \langle\Gamma\rangle_\mathrm{d}\right)^i G(\Gamma_\mathrm{d})\mathrm{d}\Gamma_\mathrm{d}$. Accordingly, the variance and the skewness of $G(\Gamma_\mathrm{d})$ can be obtained from the values of $\mu_2/\langle\Gamma\rangle_\mathrm{d}^2$ and $\mu_3/\mu_2^{3/2}$, respectively. The average decay rate, $\langle\Gamma\rangle_\mathrm{d}$, can, in practice, be fitted from the part of $\left|g^{(1)}(q,t)\right|$ that has been associated with the diffusive mode extracted from eqn (1), and is used in the following relation:

$\lim_{q\to 0, C\to 0} \langle \Gamma \rangle_{\mathrm{d}} = D_z q^2$ to obtain the *z*-average translational diffusion coefficient, D_z, under extremely dilute condition in the limit of $qR_{\mathrm{g}} < 1$. On the basis of the Stokes-Einstein relation, $\langle R_{\mathrm{h}} \rangle = k_{\mathrm{B}} T / 6\pi\eta_{\mathrm{s}} D_z$, the average hydrodynamic radius $\langle R_{\mathrm{h}} \rangle$ can thus be evaluated, where k_{B} is the Boltzmann's constant and η_{s} the solvent viscosity at the absolute temperature *T*. Herein, a similar procedure as described above was utilized to obtain the apparent hydrodynamic radius $R_{\mathrm{h,app}}$ for sample solutions of finite concentrations and for the range of scattering angles presently accessible.

2.3 Depolarized dynamic light scattering (DDLS)

To assess the peculiar relaxation feature associated with anisotropic objects, DDLS measurements utilize incident light that is vertically polarized while the scattering light is horizontally polarized after leaving the analyzer, the so-called depolarized (VH) mode. In practice, the orientation of analyzer was carefully adjusted to ensure cross alignment of the two polarized lights that yields minimum scattering intensity of toluene in the detector. Thus, the normalized field autocorrelation function is given by $\left| g^{(1)}_{\mathrm{VH}}(q,t) \right| = \exp(-\Gamma_{\mathrm{VH}} t)$, where the decay rate $\Gamma_{\mathrm{VH}} = q^2 D_{\mathrm{T}} + 6D_{\mathrm{R}}$ consisting of contributions from the translational diffusion coefficient, D_{T}, and the rotational diffusion coefficient, D_{R}. Assuming rod-like feature for the aggregate clusters, the Doi-Edwards model can be utilized to estimate the length *L* and diameter *d* by solving the following equations:[49]

$$D_{\mathrm{T}} = \frac{k_{\mathrm{B}}T\left[\ln(L/d)-\gamma\right]}{3\pi\eta_{\mathrm{s}}L} \quad (3)$$

$$D_{\mathrm{R}} = \frac{3k_{\mathrm{B}}T\left[\ln(L/d)-\gamma\right]}{\pi\eta_{\mathrm{s}}L^{3}} \quad (4)$$

where γ is a parameter weakly dependent on L/d and was fixed to be 0.3 in this study.[50]

2.4 Small angle X-ray scattering (SAXS)

SAXS measurements were performed at BL23A beamline station of the National Synchrotron Radiation Research Center (NSRRC) in Taiwan. The scattering X-ray covers a q-range of $0.06-3.7\ \mathrm{nm}^{-1}$, with 15 keV incident beam (wavelength $\lambda_0 = 0.827$ Å) and sample-to-detector distance of 3548 mm. All measurements were conducted at 25±0.1 °C.

2.5 Cryogenic transmission electron microscopy (cryo-TEM)

Specimens for cryo-TEM characterizations were prepared with a FEI Vitrobot Mark IV vitrification system at 22 °C and 100% relative humidity. A 2~5 μL drop of sample solution was put on a 300-mesh lacey carbon film supported by a copper grid, and gently blotted with filter paper for 2 s to obtain a thin liquid film on the grid. The grid was immediately plunged into liquid nitrogen and then placed in the grid holder, the temperature of which was maintained at -177 °C in the microscope. TEM imaging was conducted on a FEI Tecnai T12 TEM operated at a voltage of 120 kV.

3. Results and discussion

3.1 Bulk features of C_{60} aggregates

The DDLS analysis was first carried out to reveal the shapes of bulk C_{60} aggregates in two different solvent media, i.e., chlorobenzene and toluene. Because of the weakness of usual depolarized scattering intensity, the DDLS signal can only be clearly detected at a small scattering angle, $\theta = 30^\circ$. Fig. 1 shows the normalized intensity autocorrelation function, $g_{\mathrm{VH}}^{(2)} - 1$, at $\theta = 30^\circ$ for two different fullerene solutions at a concentration of 2 mg/mL. The $g_{\mathrm{VH}}^{(2)} - 1$ for C_{60}/chlorobenzene solution exhibits a clearly discernible relaxation pattern compared to that of C_{60}/toluene solution, which produces no discernible signals within experimental uncertainty. These features imply that while C_{60} aggregate clusters are notably anisotropic in shape in chlorobenzene, they are basically isotropic in toluene. For a similar reason, DDLS signals of 5 mg/mL fullerene solution were obtained at the scattering angles of $\theta = 30^\circ - 50^\circ$. Fig. 2a shows the normalized field autocorrelation function, $\left| g_{\mathrm{VH}}^{(1)}(q,t) \right|$, of 5 mg/mL C_{60}/chlorobenzene solution and the associated relaxation time distribution function, $A(\tau)$, as extracted from CONTIN. Two relaxation modes can be clearly identified, and the fast mode may be ascribed to the orientational motion of C_{60} aggregate clusters. Interestingly, the slow mode exhibits a q-independent relaxation which we discuss in a later section.

To analyze the orientational motion of fullerene aggregates, the average decay rate, Γ_{VH}, associated with the fast mode is plotted as a function of q^2 in Fig. 2b. In this way, the nonzero

intercept yields the value of $6D_R$ while the slope gives an estimate of D_T. Assuming eqn (3) and (4) within the rod-like picture, we obtain a mean length and diameter of L=648 nm and d=102 nm, respectively.

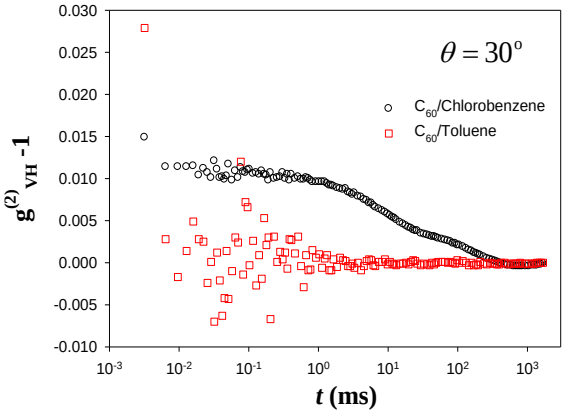

Fig. 1 Normalized intensity autocorrelation function, $g^{(2)}_{VH}-1$, at $\theta = 30^{\circ}$ for two different C_{60} solutions at a concentration of 2 mg/mL.

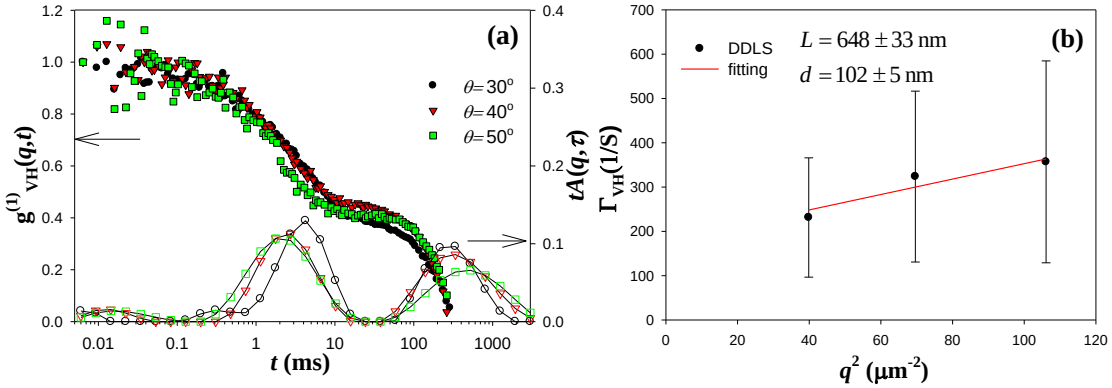

Fig. 2 (a) Angular dependences of field autocorrelation function, $\left|g^{(1)}_{VH}(q,t)\right|$, and the corresponding relaxation time distributions, $A(q,\tau)$, as extracted from CONTIN for 5 mg/mL C_{60}/chlorobenzene solution; (b) the average decay rate, Γ_{VH}, for the fast mode as a function of

q^2 , and the solid line denotes fits from eqn (3) and (4), where the fitted parameter values of L and d are indicated in the figure.

A plausible way to attest the prior DDLS analysis is to consult the cryo-TEM images, as shown in Fig. 3, which have been taken for 5 mg/mL C_{60}/chlorobenzene and 2 mg/mL C_{60}/toluene solutions. The results clearly confirm the anisotropic feature of C_{60} aggregate clusters fostered in chlorobenzene, in contrast with the isotropic objects prevalent in toluene. Note, in particular, that the sizes of C_{60} clusters evaluated from prior DDLS analysis and the cryo-TEM imaging, respectively, are in good agreement, and will be further confirmed by the results of SLS and DLS analyses discussed in a later section.

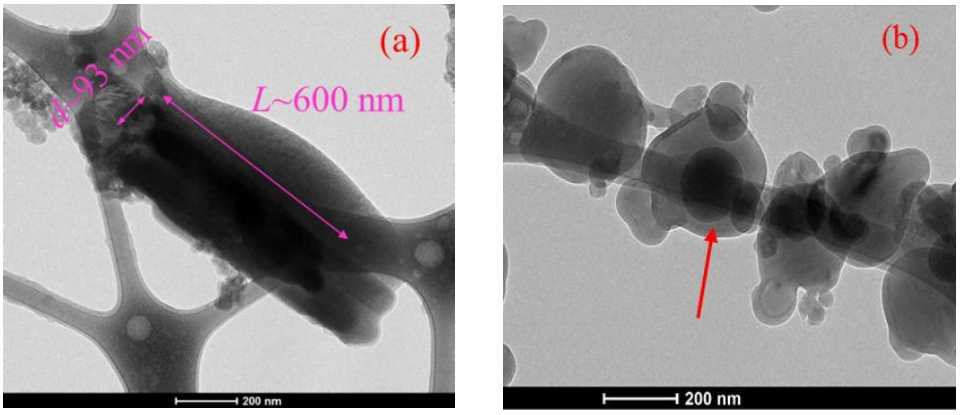

Fig. 3 Cryo-TEM images of (a) 5 mg/mL C_{60}/chlorobenzene and (b) 2 mg/mL C_{60}/toluene solutions.

3.2 Structural features of C_{60} aggregates in chlorobenzene

Prior to SLS and SAXS measurements, small angle light scattering (SALS) measurement was conducted to discriminate the presence of micrometer-sized aggregates in solution. The results revealed nearly *q*-independent SALS feature, suggesting there are no such large aggregate clusters in either solvent system of C_{60} presently investigated (see Fig. S3, ESI). In this case, combined SLS and SAXS profiles can be employed to reveal the fractal structure of C_{60} aggregate clusters and, on the other hand, the (nanoscale) structural features of the packing units.

Fig. 4 shows the SLS and SAXS intensity profiles for C_{60}/chlorobenzene solutions. Given that the results provide structural information that covers length scales from 0.3 nm to 200 nm, the analyzing scheme must invoke different physical models. First, although there is a practical gap between SLS and SAXS profiles, it is possible to bridge them using an adequate physical model as described below. Prior work on fullerene solutions suggested that SLS data can be utilized to reveal the fractal structure of C_{60} aggregate clusters.[17,19,20,51] Specifically, the polynomial formulation developed by Lin *et al.*[52] had been used to fit the SLS data and thus determine the fractal dimensions of C_{60} aggregate clusters.[17,20] At still higher q values corresponding to the Porod regime, $I(q) \sim q^{-4}$ (i.e., 0.06 < q (nm^{-1}) < 0.25), the results become inaccessible by typical SLS analysis. This regime marks the onset of "seeing" the

surface property of C_{60} aggregate clusters[53] and, moreover, is essential to decipher features of the (interior) fractal network.

On the basis of prior DDLS analysis suggestive of the formation of anisotropic fullerene aggregate clusters in chlorobenzene, the form factor of randomly oriented cylinders (with radius *R* and length *L*), $P_{\mathrm{cyl}}(q)$, is utilized:

$$P_{\mathrm{cyl}}(q) = \int_0^{\pi/2} \left[\frac{\sin(\frac{1}{2} qL\cos\phi)}{\frac{1}{2} qL\cos\phi} \frac{2J_1(qR\sin\phi)}{qR\sin\phi} \right]^2 \sin\phi \, \mathrm{d}\phi \qquad (5)$$

where $J_1(x)$ is the Bessel function of the first kind. For polydisperse cylinders, the *z*-averaged length-polydisperse form factor, $I_{\mathrm{SLS}}(q) \sim n\Delta\rho^2 V_{\mathrm{P}}^2 P_{\mathrm{Z}}(q)$, should be used.[54] In this expression, *n* denotes the number density of C_{60} aggregates, $\Delta\rho$ the refractive index contrast, and V_{p} the volume of each fullerene aggregate; $P_{\mathrm{Z}}(q)$ denotes the *z*-averaged form factor and is given by

$$P_{\mathrm{Z}}(q) = \frac{\int_0^\infty L\, w(L) P_{\mathrm{cyl}}(q)\, dL}{\int_0^\infty L\, w(L)\, dL} \qquad (6)$$

where *w*(*L*) is Zimm-Schulz-Flory distribution and bears a form

$$w(L) = \frac{L^z}{\Gamma(z+1)} \left(\frac{z+1}{L_{\mathrm{w}}}\right)^{z+1} \exp\left(-\frac{z+1}{L_{\mathrm{w}}} L\right) \qquad (7)$$

In eqn (7), Γ(*x*) denotes the gamma function, L_{w} the weight-averaged length of the cylinders, L_{n} the number-averaged length, and $z^{-1} = L_{\mathrm{w}}/L_{\mathrm{n}} - 1$. These parameters may be associated with the polydispersidy index (PDI) as $\mathrm{PDI} = L_{\mathrm{w}}/L_{\mathrm{n}} = z^{-1} + 1$. Herein, *n*, V_{p} and $\Delta\rho$ were treated as adjustable parameters, which have no effect on the *q* dependence of the form factor, as the main purpose of the fitting was to determine the geometrical parameter L_{w}.

The other parameter, R, can be independently evaluated by a linear fit of ln $I(q)q$ vs. q^2 plot. The plot exhibited a fair straight line indicative of nearly monodisperse cross-sectional dimension, and accordingly the value of R can be determined with precision (see Fig. S4, ESI). To simultaneously fit the SLS and SAXS curves, the SLS profile must be shifted along the vertical axis so that the q value, at which the scaling law of $I_{SLS}(q)\sim q^{-1}$ intersects with that of $I_{SAXS}(q)\sim q^{-4}$, matches the reciprocal of $R_{g,R}$ (the radius of gyration of R); see Fig. S4 in ESI. Note also that the values of L_w for three different C_{60} concentrations were found to be insensitive to the choice of z in the range of 0.001 to 0.1 (see Fig. S5, ESI).

The fitting is displayed by the dashed line in Fig. 4, and the prediction captures a smooth transit to the Porod regime. The geometrical parameters used in the fitting for C_{60}/chlorobenzene solutions are provided in Table 1. It can be seen that the geometrical features so determined compare favorably with the results of prior DDLS and cryo-TEM analyses. Before we proceed further to the high-q SAXS data, it should be noted that the scattering intensity profile in the range of q (nm^{-1}) >1 differs substantially between C_{60}/chlorobenzene and C_{60}/toluene solutions, as shown in Fig. 5, and therefore must require different analyzing schemes as introduced below.

For the SAXS data on C_{60}/chlorobenzene solutions, the scattering intensity starts to exhibit an upturn approximately in the range of $0.25< q$ (nm^{-1}) < 0.4. This feature indicates the scattering intensity in this region is contributed by not only the form factor of the packing units

but also the fractal objects that embody them. At still higher q, isolated C_{60} molecules might also contribute to the scattering intensity[55] (cf. the contributions of small C_{60} clusters such as dimers were not considered, however, according to the observation discussed with Fig. S6 in ESI). Thus, the full range of SAXS data at q (nm^{-1}) > 0.25 may be analyzed using a combination of (fractal) structure factor and (packing unit) form factor plus the contribution of isolated C_{60} molecules: $I_{\mathrm{SAXS}}(q) \sim P_{\mathrm{unit}}(q)S(q) + I_{\mathrm{single}}(q)$. The scattering intensity of single C_{60} molecules can be assessed by $I_{\mathrm{single}}(q) = n_{\mathrm{single}}(\Delta\rho_{\mathrm{single}})^2 V_{\mathrm{single}}^2 P_{\mathrm{single}}(q)$, where n_{single} denotes the number density of isolated C_{60} molecules, $\Delta\rho_{\mathrm{single}}$ the difference in scattering length density between fullerene and the solvent medium, V_{single} and $P_{\mathrm{single}}(q)$ the volume and form factor of single C_{60} molecule, respectively.[56] The suitable form factor for the packing units can be judged by the anisotropic rod-like structure with a scaling exponent of -1[48] as observed in Fig. 5 at q (nm^{-1}) > 1. Thus, $P_{\mathrm{unit}}(q)$ was taken to be the from factor of cylinders as given by eqn (5) as well. A rather general expression of $S(q)$ describing the fractal structure within an (bounded) aggregate cluster is considered:[19,57]

$$S(q) = 1 + \frac{1}{(qR_{\mathrm{e}})^D} \frac{D\Gamma(D-1)}{\left(1 + (q\xi)^{-2}\right)^{(D-1)/2}} \sin\left[(D-1)\arctan(q\xi)\right] \qquad (8)$$

where D is the fractal dimension; ξ is the cut-off length marking the boundary of an aggregate cluster or, more generally, (colloidal) network system beyond which the mass distribution is no longer described by the fractal law, and thus it is expected to bear magnitude comparable with the mean size of C_{60} clusters; R_{e} is expected to reflect the dimension of the packing units.

As shown in Table 1, the mean sizes of fractal aggregates as calculated from ξ (i.e., R_g_$S(q)$) are in reasonable agreement with the results from prior form factor analysis (i.e., R_g_cyl) for C_{60}/chlorobenzene solutions. In both cases, a notable increase in the mean aggregate size can be observed only at a relatively high concentration c = 5mg/ml. The fractal dimension D, generally falling in the range of 2.8 ~ 3, also increases slightly at a higher concentration, suggestive of the formation of increasingly more compact C_{60} aggregates. Given that the fractal dimensions are notably greater than the predictions (~2) based on cluster-cluster aggregation mechanism, the scenario of monomer (or, in the present case, packing unit)-cluster interactions seems to better describe the present data.[58] Finally, the mass fraction (i.e., n_{single}/c) of single C_{60} molecules in chlorobenzene was determined to lie between 0.35 and 0.45, slightly below what had been estimated by computer simulation for PCBM solutions.[59] Coexistence of molecular fullerenes and colloidal aggregates had previously been noted for aqueous solution systems.[60-62] Besides, the results indicated that the mass fraction of molecularly dispersed C_{60} first increases with increased C_{60} concentration and then quickly reaches a constant value of about 0.45 at c=2 mg/mL—a possible indication of an analogous critical-micelle-concentration (CMC) transition.[63]

Overall, the analyses combing SLS and SAXS profiles have led to a relatively complete and more detailed picture of C_{60} clusters incubated in chlorobenzene, as depicted in Fig. 6. An interesting feature is that the overall cylinder-like cluster is itself composed by self-similar,

anisotropic packing units. A similar conclusion, in fact, was reached for the counterpart C_{60}/toluene solutions discussed shortly, differing only in that the packing unit and the bulk cluster assume an (spherical) isotropic shape in the latter system. Similar contrasting (i.e., isotropic vs. anisotropic packing) features had also been reported with C_{60} and C_{70} in acetonitrile–benzonitrile solvent mixtures,[22] as well as for curcumin particles in solution under the influence of various types of surfactants.[64] Presumably, the side-side van der Waals interaction of anisotropic packing units would be energetically favorable, and the cluster subsequently grows as a result of such anisotropic packing; see also a later discussion in view of the effect of solvent quality.

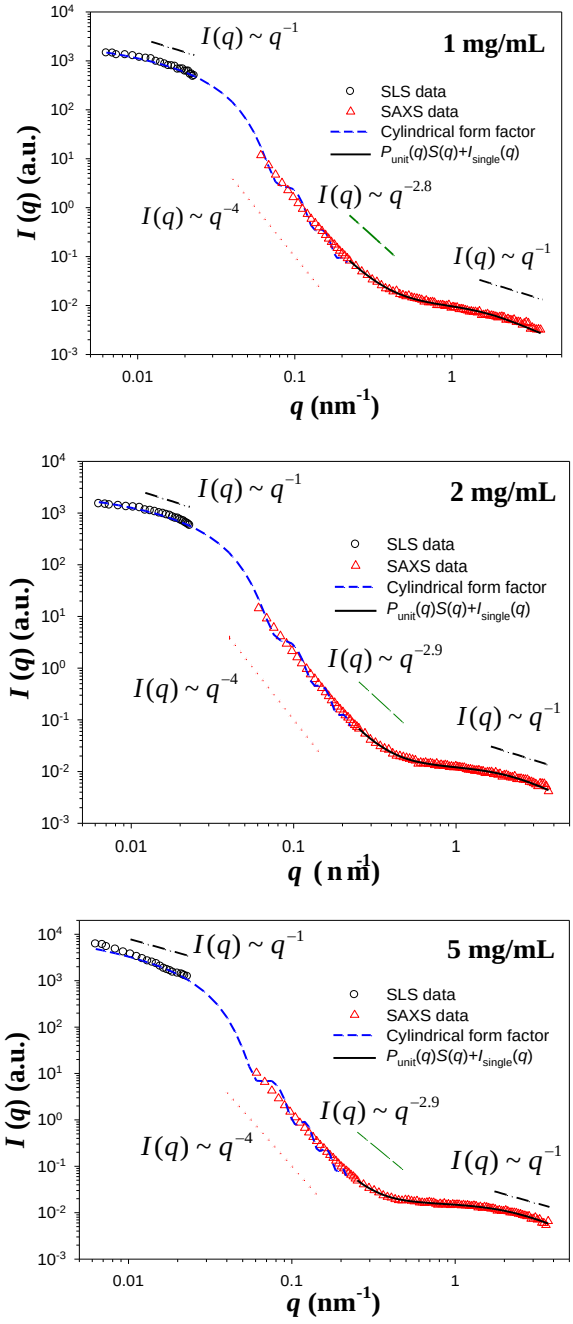

Fig. 4 Combined SLS and SAXS intensity profiles for 1 mg/mL, 2 mg/mL, and 5 mg/mL C_{60}/chlorobenzene solutions, respectively. The dashed line denotes the fitting with eqn (5)-(7) with z=0.01, and the solid line (for q (nm^{-1}) > 0.25) the fitting with eqn (5) and (8) plus $I_{\text{single}}(q)$.

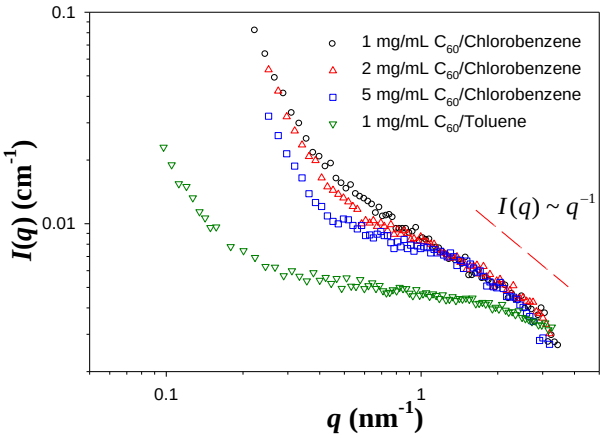

Fig. 5 SAXS intensity profiles (after subtracting the contribution of isolated C_{60} molecules) for C_{60}/chlorobenzene and C_{60}/toluene solutions, respectively. To better discern different scaling behaviors at high *q*, data have been vertically shifted by various amounts.

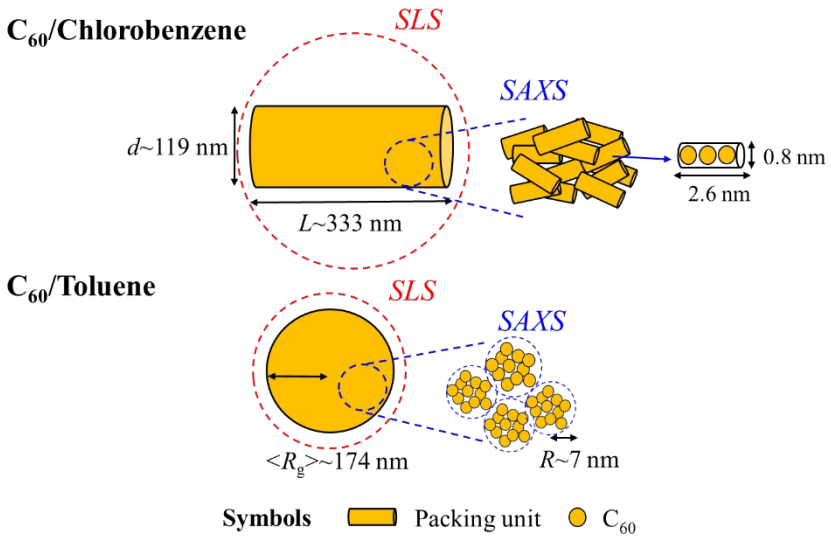

Fig. 6 Schematic illustrations of a hierarchy of structural features of C_{60} clusters incubated in two different solvent media at a representative concentration of 1 mg/mL.

Table 1 Fitted structural parameters for aggregate clusters in C_{60}/chlorobenzene solutions

Concentration	1 mg/mL	2 mg/mL	5 mg/mL
Length of rod-like structure (L_w) [nm][a]	333.1	287.4	663.4
Radius of rod-like structure (R) [nm]	59.7±22.1	59.7±2.4	75.6±3.9
z[a]	0.01	0.01	0.01
R_g_cyl [nm][b]	105.0	93.1	198.8
Length of packing unit [nm][c]	2.57±0.02	2.05±0.02	2.06±0.02
Radius of packing unit [nm][c]	0.38±0.01	0.36±0.01	0.42±0.01
Fractal dimension (D)[c]	2.83±0.02	2.93±0.02	2.98±0.02
Cut-off length (ξ) [nm][c]	33.1±0.1	31.6±0.1	48.9±0.2
Effective radius of packing unit (R_e) [nm][c]	2.4±0.1	2.3±0.1	2.3±0.1
n_{single} [mg/mL][d]	0.36	0.93	2.01
R_g_$S(q)$ [nm][e]	77.1	75.7	119.6

[a] Obtained from SLS and SAXS data fitted using eqn (5)-(7). [b] Calculated from the relation $R_g^2 = L_w^2/12 + R^2/2$. [c] Obtained from SAXS data fitted from the relation $I(q) \sim P_{unit}(q)S(q) + I_{single}(q)$. [d] Obtained from $I_{single}(q) = n_{single}(\Delta\rho_{single})^2 V_{single}^2 P_{single}(q)$. [e] Calculated from the relation $R_g\_S(q) = [D(D+1)/2]^{0.5}\xi$.

3.3 Structural features of C_{60} aggregates in toluene

The DDLS feature in Fig. 1 indicated that C_{60} clusters incubated in toluene assume a basically isotropic shape. Fig. 7 shows the corresponding SLS data can be well described by the form factor of spheres accounting for a moderate polydispersity in radius:

$$P(q) = I(q)/I(0) = \frac{\int_0^\infty G_n(R)\alpha^2(R)P(qR)\mathrm{d}R}{\int_0^\infty G_n(R)\alpha^2(R)\mathrm{d}R} \quad (9)$$

where $G_n(R)$ is the number-weighted distribution of the radius R of aggregate clusters, $\alpha(R)$ is the polarizability and may be expressed by $\alpha(R) \propto R^\gamma$;[65] for spherical particles, γ=3 and $P(qR) = \left[3(\sin qR - qR\cos qR)/(qR)^3\right]^2$. The fitted results of $G_n(R)$ are shown in the inset of Fig. 7, with a PDI ~2. The fitting (dashed line) is seen to reasonably bridge the SAXS data in the low-q region (i.e., q (nm^{-1}) <0.1) after an arbitary vertical shift of the SLS data. Interestingly, the Porod regime was not clearly observable for C_{60}/toluene solutions in contrast with the C_{60}/chlorobenzene solutions discussed previously, namely, there is no conspicuous q^{-4} dependence in the intermediate-q region; see also Fig. 5 for comparison. The lack of the Porod regime for C_{60}/toluene solutions could be indicative of a less smooth cluster surface or clusters constituted by larger packing units.[66] Moreover, the varied SAXS profiles at q (nm^{-1}) >0.25 as is evident in Fig. 5 suggest that the internal (fractal plus packing unit) structures in the two solvent systems must differ in certain ways, as discussed below.

First, the scattering intensity exhibits an upturn in the region of 0.08< q < 0.25 indicative of the existence of a fractal structure. This is also the region that ceases to be described by the

form factor for bulk C_{60} clusters. Despite the fact that the upturn is less pronounced at a higher concentration of 2 mg/mL, fractal aggregates had been reported in prior light scattering study for C_{60}/toluene solutions at similar and higher concentrations.[19] Due in part to this observation, the following discussion is focused on the case with 1 mg/mL. We again utilize the combined formula $I_{\mathrm{SAXS}}(q) \sim P_{\mathrm{unit}}(q)S(q) + I_{\mathrm{single}}(q)$ to simultaneously capture the fractal structure and, in the high-q region, geometrical features of the building units, where $S(q)$ represents the (fractal) structure factor as given by eqn (8). Lacking the -1 scaling behavior as previously observed with C_{60}/chlorobenzene solutions, the form factor of spheres (but not for cylinders which have been noticed to work poorly) for $P_{\mathrm{unit}}(q)$ was found to describe fairly well the SAXS data in the high-q region. The fitting is displayed by the solid line superimposed on the experimental data in Fig. 7, and the structural parameter values so obtained are gathered in Table 2.

It can be seen that the mean size of C_{60} clusters (i.e., $\langle R \rangle$) in toluene as evaluated from the SLS data is in fairly good agreement with what has later been retrieved from the SAXS data (i.e., $R_{g\_}S(q)$). The fractal dimension, ~2.7, is only slightly smaller than those previously found for C_{60}/chlorobenzene solutions. In contrast, the mass fraction of single C_{60} molecules in toluene (~0.23) is considerably smaller than those in chlorobenzene indicative of a poorer solvent quality for the former medium. In the SAXS analysis, we have also noticed that the size of the packing units as determined from the structure factor $S(q)$ (R_e~7 nm) is notably

greater than that evaluated from the associated form factor $P_{\text{unit}}(q)$ (R_0 ~0.5 nm). Prior work on C_{60}/toluene solutions of a similar concentration suggested that C_{60} may form aggregates with size up to ~5 nm,[67] and that the fractal clusters are built up by small aggregates with size of ~6 nm.[68] The reason that the form factor analysis yields a much smaller value for R_0 can be ascribed to a relatively flat SAXS profile at high q. Note, however, that if the effect of interparticle interferences *within* a packing unit was at work in the region of $qR_e>1$,[69] the true value of R_0 might be substantially underestimated by considering only the form factor contribution. A similar comparison, in fact, has been noticed with C_{60}/chlorobenzene solutions, although the disparity is less pronounced. Illustrations of a hierarchy of aggregate features in C_{60}/toluene solution can also be found in Fig. 6.

Overall, we have shown that DDLS, SLS, SAXS, and cryo-TEM analyses consistently revealed distinct features of C_{60} aggregate clusters that have been fostered in chlorobenzene and toluene, respectively. Previously, the effect of solvent quality had been observed in computer simulation indicating that PCBM aggregates are three-dimensional (3D) by nature in o-dichlorobenzene and are close to 2D in chlorobenzene.[59] In either case, the knowledge gained should help one fabricate solvent-tunable morphologies of fullerene aggregates. Below, we provide a simple interpretation of such disparity from the perspectives of solvent quality and interfacial energy. For a better solvent such as chlorobenzene (judged by its higher solubility for C_{60}), C_{60} is encouraged to form clusters with shapes that deviate substantially from the

spherical one, which yields the minimum specific surface exposed to the solvent medium. This trend might explain why C_{60} forms rod-like clusters in chlorobenzene yet isotropic ones in toluene, the latter being much poorer solvent than the former. Indeed, prior work had indicated that while one fullerene derivative with a high solubility in aqueous solution forms long rods, another less soluble one forms spherical droplets.[33] Of course, this simple argument on surface energy would, at best, capture the thermodynamic aspect of the solution systems under investigation, offering virtually no account of the kinetic factors that can also play an important role in aggregate formation. It is worth noting that optical microscopy (OM) and scanning electron microscopy (SEM) imaging of drop-casting thin films also revealed contrasting features of the aggregate morphology of C_{60}; see Fig. S7 in ESI. Specifically, while the micron-scale aggregates produced from chlorobenzene medium assume a notably branched structure, those created from the toluene medium assume purely cylindrical or rod-like shape. Moreover, the XRD patterns of thin film shown in Fig. S8 in ESI revealed distinct crystal structures, suggesting that different solvent media can be utilized to control both crystal structure[70,71] and aggregate shape.[72] Unfortunately, the present study can render no further clues to the possible connection between these states. Solution-state dependences of thin film aggregate structures and morphologies had been observed for a wide range of material systems including colloids,[64,73,74] amphiphilic block copolymers,[75] polymer composites,[35] and biological

polymers.[76] In this respect, it seems that much remains to be explored for the case with fullerene solutions and thin films.

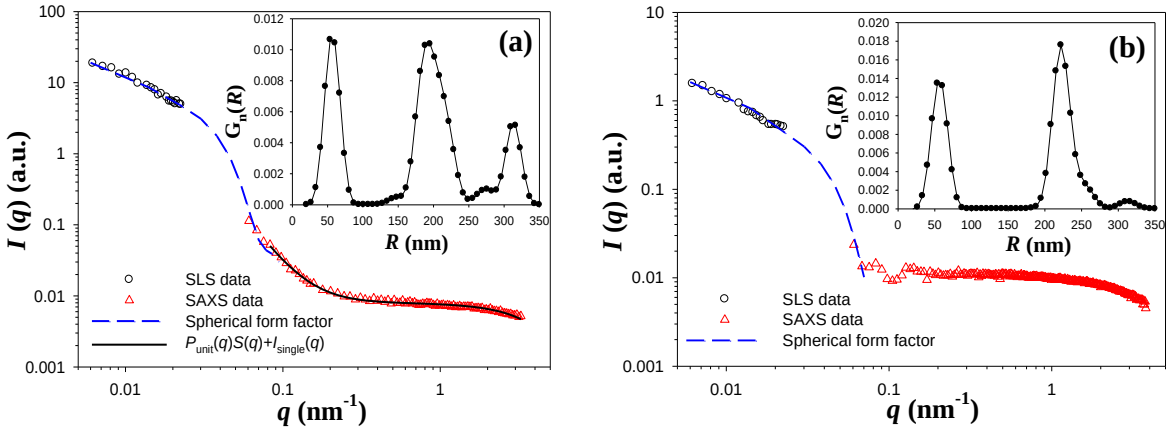

Fig. 7 Combined SLS and SAXS intensity profiles for (a) 1 mg/mL and (b) 2 mg/mL C_{60}/toluene solutions, where the insets show the number-weighted size distributions as have been extracted from the fitting with eqn (9). The dashed line in both cases denotes fitting with eqn (9), while the solid line in (a) represents fitting with eqn (8) along with the form factor of spheres and $I_{\text{single}}(q)$.

Table 2 Fitted structural parameters for aggregate clusters in C_{60}/toluene solutions

	1 mg/mL	2 mg/mL
Average radius of fullerene aggregate (<*R*>) [nm][a]	174±88	162±86
Radius of primary particles (R_0) [nm][b]	0.51 ±0.01	-
Fractal dimension (D)[b]	2.71±0.02	-
Correlation length (ξ) [nm][b]	84.6±0.5	-
Effective radius of packing unit (R_e) [nm][b]	7.3±0.1	-
n_{single} [mg/mL] [c]	0.23	-
$R_g\_S(q)$ [nm][d]	190	-

[a] Fitted from SLS data and the low-q part of SAXS data using eqn (9). [b] Obtained from SAXS data fitted using the expression $I(q) \sim P_{unit}(q)S(q) + I_{single}(q)$. [c] Obtained from $I_{single}(q) = n_{single}(\Delta\rho_{single})^2 V_{single}^2 P_{single}(q)$. [d] Calculated from the relation $R_g\_S(q) = [D(D+1)/2]^{0.5}\xi$.

3.4 DLS features

The DLS data on C_{60} solutions exhibit complex features that deserve special attention. Before we discuss the essential features and their possible physical meanings, it should be reminded that the present DLS experiments were conducted using a long-wavelength incident light that avoids the common problems associated with absorption. Furthermore, we noticed that the individual measurement yielded $g^{(2)}(q,t)$ curve that was typically fraught with wide fluctuations.

Therefore, all the results reported herein on $\left|g^{(1)}(q,t)\right|$ have capitalized on the average of $g^{(2)}(q,t)$ over 10 to 20 independent runs.

For both solvent systems of C_{60}, the field autocorrelation function $\left|g^{(1)}(q,t)\right|$ ubiquitously embodies two relaxation modes (i.e., fast- and slow-mode) for all concentrations investigated, as shown in Fig. 8 and 9. Fig. 8 shows the detailed curves of C_{60}/chlorobenzene solutions along with the relaxation time distributions $A(q,\tau)$ extracted from CONTIN. First, the scaling relation $\langle\Gamma_i\rangle \sim q^{\alpha}$ has been utilized to reveal the attribute of each individual mode. The value of α for the fast mode is close to 2 indicative of translational motions, whereas the slow mode exhibits a nearly q-independent relaxation (i.e., $\alpha \sim 0$), as shown in the insets of Fig. 8. Given that the physical meaning of the slow mode remains unclarified, we focus mainly on the analysis of the fast mode and, afterward, briefly comment on the significance of the slow mode.

Expecting the rotational motion of a rod-like aggregate may contribute to the isotropic (VV) spectral distribution (i.e., $\left|g^{(1)}(q,t)\right|$) when lying in the range of $qL>3$,[77] as is the case with the present C_{60}/chlorobenzene solutions, we utilized the first cumulant to account for such an effect,[49,50] namely, $\langle\Gamma\rangle_{\mathrm{d}} = 3D_{\mathrm{G}}q^2/2$ in eqn (2) for describing the $\left|g^{(1)}(q,t)\right|$ associated with the fast mode, where D_{G} is the diffusion coefficient of the mass center of a rod-like aggregate and is given by $D_{\mathrm{G}} = k_{\mathrm{B}}T\left[\ln(L/d)-\gamma\right]/3\pi\eta_{\mathrm{s}}L$. The theoretical fitting is displayed by solid lines in Fig. 8 along with the DLS data. The mean length and diameter of rod-like aggregates so evaluated from the cumulant expansion, as listed in Table 3, can be seen to be in

generally good agreement with the geometrical parameters obtained earlier from SLS and DDLS analyses. In addition, the ρ-ratio (R_g/R_h) that yields information of the morphological features of C_{60} clusters is also in good agreement with the theoretical prediction of $\ln(L/d-0.5)/\sqrt{3}$,[48] also shown in Table 3, as the values of L and d determined from SLS and DLS experiments, respectively, were utilized to set a theoretical range of ρ-ratios. The general agreement is important to solidify the present analyses on C_{60} solutions.

For C_{60}/toluene solutions, Fig. 9 shows the field autocorrelation function $\left|g^{(1)}(q,t)\right|$ also exhibits two relaxation modes. Similarly, the fast mode might be attributed to the diffusive motion, although the scaling exponent appears to deviate more significantly from the expected value of $\alpha = 2$. The deviations could be due to the effect of polydispersity in aggregate size as well as its proximity to the second (q-independent) mode, which we discuss shortly. Using eqn (2) with the relation $\langle\Gamma\rangle_d = D_z q^2$, the mean apparent hydrodynamic radius ($R_{h,app}$) can be obtained by fitting $\left|g^{(1)}(q,t)\right|$ associated with the fast mode. As shown in Table 3, the $R_{h,app}$ of C_{60} clusters for 2 mg/mL C_{60}/toluene solution is in good agreement with a previous report (cluster sizes of 50~200 nm).[19] Moreover, the ρ-ratios for C_{60}/toluene solutions are basically described by the theory for homogeneous spheres (i.e., 0.775), indicative of spherical and colloid-like attribute of C_{60} aggregates in toluene.

A second, slow mode was observed for both C_{60}/chlorobenzene and C_{60}/toluene solutions. Prior studies had suggested this mode may be attributed to the formation of large C_{60}

aggregates.[19,29,78] In this study utilizing multi-angular light scattering, the slow mode was identified to exhibit a nearly *q*-independent relaxation, $\langle\Gamma\rangle \sim q^0$. This scaling behavior had been ascribed to, for instance, chain conformational relaxation[79] and stronger segmental interaction near the entanglement nodes.[80] More generally, this essential DLS feature seems to involve either elastic responses due to the formation of physical bonds, or chain relaxations subject to physical confinements.[81] The latter implication is of particular interest, because a similar argument may, in principle, apply to any confined motions of polymer chains or particulate molecules, as manifested by recent computer simulations.[82]

To assess this possibility (i.e., the effect of confinement) for the presently identified slow-mode relaxations of C_{60} solutions, we have analyzed the number density of C_{60} aggregates, ν, in solution. The value of ν for a given concentration can be estimated through the basic relation $\nu = cN_A / M$, where c and N_A are the C_{60} concentration (after the subtraction of isolated C_{60} molecules) and the Avogadro's number, respectively; M denotes the molecular weight of a single C_{60} cluster with a mean radius of R, and may be estimated via the relation $M = M_{R_e} \times 4.46 D^{-2.08} (R/R_e)^D$,[83] where M_{R_e} is the molecular weight of a building unit with radius R_e. Detailed calculations can be found in Table S1 in ESI. It was found that the number density of C_{60} clusters for C_{60}/chlorobenzene solutions clearly has reached the semidilute regime, where rod overlapping becomes pronounced and the hindrance of rotational motion at long times can be expected. Accordingly, a "tube diameter" defining the confining space has

been estimated to fall in the range of 200 to 500 nm (see Table S2 in ESI), which indeed is considerably smaller than the previously determined rod length *L* in most cases. Recall that the slow mode extracted from prior DDLS results also displayed a nearly *q*-independent relaxation for 5 mg/mL C_{60}/chlorobenzene solution, as can be seen in Fig. 2. In particular, the relaxation time τ observed in the DLS experiment is close to that observed in the DDLS experiment, suggesting the slow mode in both experiments may be ascribed to a confined diffusion of anisotropic aggregate clusters through the tunnels defined by the surrounding clusters.

The story for C_{60}/toluene solutions seems to be more complicated, though, as a similar estimate in the number density revealed a dilute condition for the aggregate clusters. Still, a generally broad aggregate size distribution as has been noted with this solution system could easily bring in local confinements for some prodigious clusters, thus contributing to a similar *q*-independence in the DLS response. In summary, the present DLS (and some DDLS) features on dilute/semidilute C_{60}/chlorobenzene and C_{60}/toluene solutions revealed interesting *q*-independence for the long-time slow mode that had not been reported in prior work on fullerene solutions. Given that the SALS analysis shown in Fig. S3 in ESI suggested there was no micrometer-sized aggregate species in both solution systems, this peculiar DLS feature could signify a short-time, confined (1-D) diffusion of C_{60} aggregate clusters. Nevertheless, the analysis remains inconclusive, especially for C_{60}/toluene solutions, and must await future corroborations.

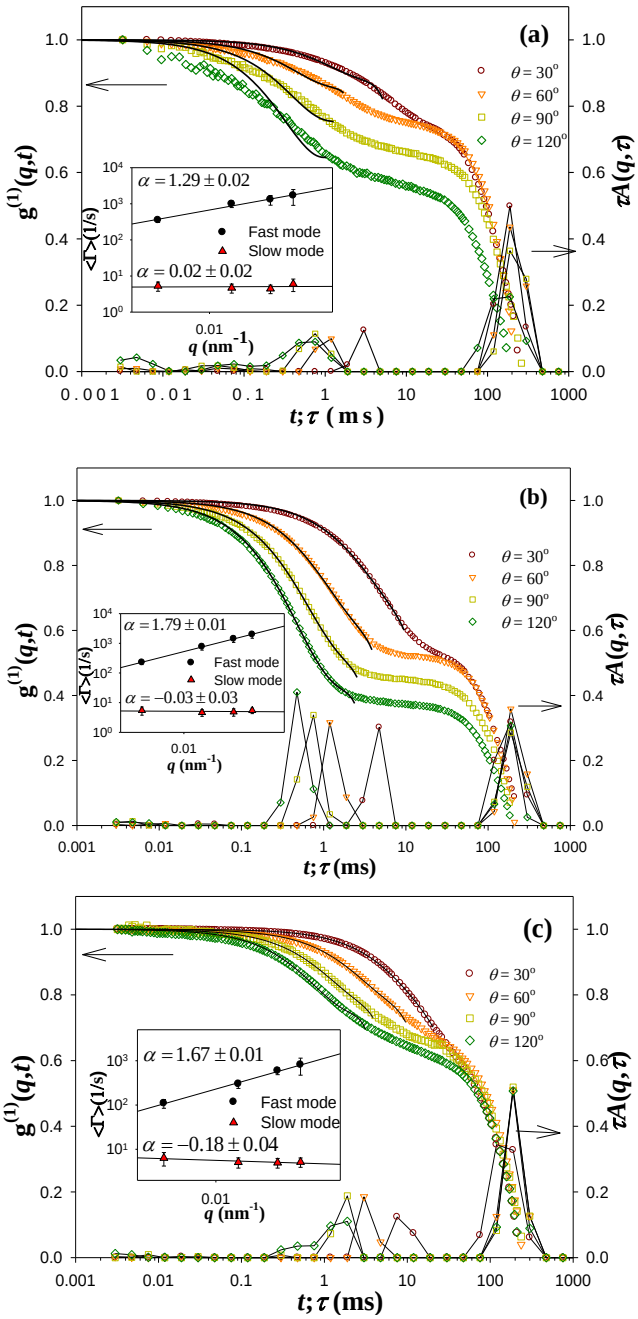

Fig. 8 Angular dependences of field autocorrelation function $\left|g^{(1)}(q,t)\right|$ and relaxation time distributions $A(q,\tau)$ retrieved from CONTIN for (a) 1 mg/mL, (b) 2 mg/mL, and (c) 5 mg/mL C_{60}/chlorobenzene solutions, where the solid lines represent the fitting with eqn (2) for the part of fast-mode relaxation. The decay rates $\langle\Gamma_i\rangle$ extracted from the relaxation time distribution $A(q,\tau)$ as a function of q for two characteristic relaxation modes are shown in the inset.

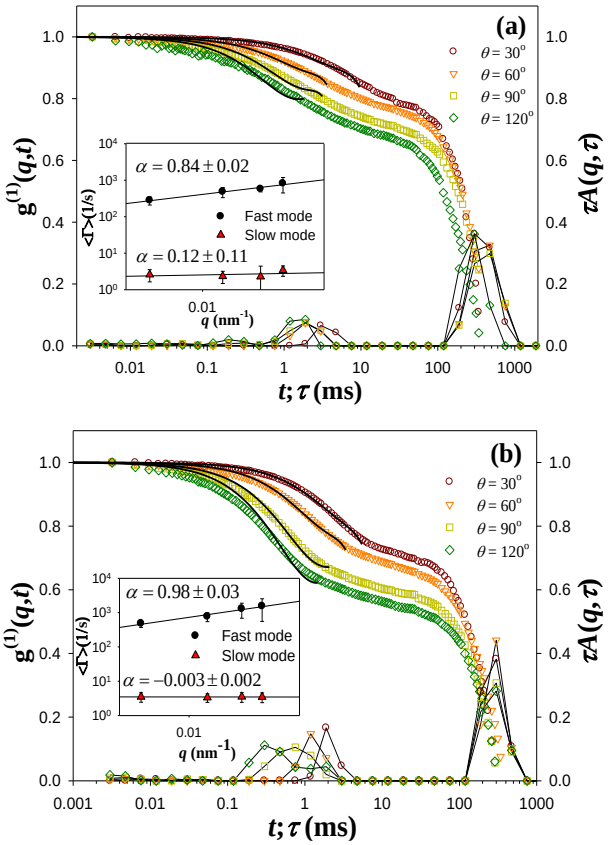

Fig. 9 Angular dependences of field autocorrelation function $\left|g^{(1)}(q,t)\right|$ and relaxation time distributions $A(q,\tau)$ retrieved from CONTIN for (a) 1 mg/mL and (b) 2 mg/mL C_{60}/toluene solutions, where the solid lines represent the fitting with eqn (2) for the part of fast-mode relaxation. The decay rates $\langle\Gamma_i\rangle$ extracted from the relaxation time distribution $A(q,\tau)$ as a function of q for two characteristic relaxation modes are shown in the inset.

Table 3 Parameter values extracted from DLS analyses of various C_{60} solutions

sample	Length (L) [nm][a]	Diameter (d) [nm][a]	R_h_cyl [nm][b]	$R_{h,app}$ [nm][c]	ρ–ratio	Theoretical ρ–ratio
1 mg/mL C_{60}/chlorobenzene	424±63	98±12	182	-	0.58[d]	0.48~0.77[f]
2 mg/mL C_{60}/chlorobenzene	377±50	88±6	162	-	0.57[d]	0.37~0.76[f]
5 mg/mL C_{60}/chlorobenzene	642±98	290±37	650	-	0.31[d]	0.31~0.78[f]
1 mg/mL C_{60}/toluene	-	-		424±55	0.41[e]	0.775
2 mg/mL C_{60}/toluene	-	-		186±37	0.87[e]	0.775

[a] Retrieved from $\left|g^{(1)}(q,t)\right|$ associated with the fast mode using eqn (2) and $\langle\Gamma\rangle_d = 3D_G q^2/2$, further averaged over the results obtained from four different scattering angles. [b] Calculated from the relation $R_h = L/2\left[\ln(L/d)-0.3\right]$. [c] Retrieved from $\left|g^{(1)}(q,t)\right|$ associated with the fast mode using eqn (2) and $\langle\Gamma\rangle_d = D_z q^2$, further averaged over the results obtained from four different scattering angles. [d] Calculated from R_g_cyl/ R_h_cyl. [e] Calculated from $\langle R\rangle/R_{h,app}$. [f] Calculated from the prediction of $\ln(L/d-0.5)/\sqrt{3}$ with L and d obtained from SLS or DLS analysis that yields a range of ρ–ratios.

4. Conclusions

This study explored the mesoscale aggregation properties of C_{60} clusters and their building units in two distinct solvents and a practical range of concentrations, with an aim to understand the use of different types of organic solvents by which to engineer the structural and morphological features of (stabilized) colloidal aggregates under conditions which can be easily implemented in recent applications with organic electronics. The central observations were as follows: (1) Mean aggregate sizes of C_{60} clusters in the range of several hundred nanometers have been independently revealed by SLS, DLS, and DDLS analyses for both solvent systems. (2) DDLS and cryo-TEM measurements further revealed that while C_{60} aggregates fostered in chlorobenzene are notably anisotropic (rod-like), they are basically isotropic (spherical) in toluene. In both cases, the features of ρ-ratio (R_g/R_h) of C_{60} clusters as evaluated from combined SLS/DLS analyses are in good agreement with the theoretical predictions for colloidal particles of varying shape. (3) SAXS data indicated cylinder-like, anisotropic packing units for C_{60} clusters in chlorobenzene, and sphere-like units that are relatively large in size in toluene. The combined features of (2) and (3) implied there exists striking self-similarity between the aggregate clusters and their building units. (4) In all cases, SAXS analysis clearly indicated there was a certain (mass) fraction (0.35~0.45 in chlorobenzene and 0.23 in toluene) of molecularly dispersed C_{60} coexistent with the colloidal aggregates noted above. The long-term stability of these colloidal and molecular species of C_{60}

as well as their interplay is yet to be explored. (5) The features in (3) and (4) confirmed the relative superiority of solvent quality of the two solvent media investigated, in accord with known solubility data reported in the literature. The results implied that a relatively good solvent (i.e., chlorobenzene in the present case) results in more stabilized colloidal C_{60} solutions along with a higher fraction of molecularly dispersed C_{60} and, possibly, might be utilized to incubate anisotropic aggregate clusters. (6) From the dynamic perspective, DLS signals clearly displayed two distinct relaxation modes (fast- and slow-mode) for both solution systems. While the fast mode is basically diffusive by nature, the slow mode, which exhibits nearly q independent behavior, was tentatively attributed to the effect of mutual confinements according to our number density analysis. The analysis, however, remains inconclusive and should benefit from future work on a wider variety of fullerene solutions. (7) SEM/OM images and XRD patterns of drop-casting thin films revealed a clear dependence of the (micron-scale) aggregate morphology and (local) crystal structure on their prior features in solution state. The correlation—which notably prevails over a hierarchy of length scales—sheds light on the possibility to engineer the solution aggregation properties of fullerene in order to produce thin films with tunable structural and morphological features for current nanotechnological applications.

Acknowledgements

The authors thank the reviewers for useful suggestions leading to a general improvement of this article. This work was sponsored by the Ministry of Science and Technology of ROC. We acknowledge NSRRC of ROC for facilitating the SAXS experiments.

References

1 H. Li, B. C. Tee, J. J. Cha, Y. Cui, J. W. Chung, S. Y. Lee and Z. Bao, *J. Am. Chem. Soc.*, 2012, **134**, 2760-2765.
2 J. L. Segura, N. Martin and D. M. Guldi, *Chem. Soc. Rev.*, 2005, **34**, 31-47.
3 S. S. Babu, H. Mohwald and T. Nakanishi, *Chem. Soc. Rev.*, 2010, **39**, 4021-4035.
4 P. Mroz, G. P. Tegos, H. Gali, T. Wharton, T. Sarna and M. R. Hamblin, *Photochem. Photobiol. Sci.*, 2007, **6**, 1139-1149.
5 L. K. Shrestha, Q. Ji, T. Mori, K. Miyazawa, Y. Yamauchi, J. P. Hill and K. Ariga, *Chem. Asian. J.*, 2013, **8**, 1662-1679.
6 J.-I. Minato and K. Miyazawa, *Carbon*, 2005, **43**, 2837-2841.
7 H. Liu, Y. Li, L. Jiang, H. Luo, S. Xiao, H. Fang, H. Li, D. Zhu, D. Yu, J. Xu and B. Xiang, *J. Am. Chem. Soc.*, 2002, **124**, 13370-13371.
8 H.-X. Ji, J.-S. Hu, Q.-X. Tang, W.-G. Song, C.-R. Wang, W.-P. Hu, L.-J. Wan and S.-T. Lee, *J. Phys. Chem. C*, 2007, **111**, 10498-10502.
9 J. Jeong, W.-S. Kim, S.-I. Park, T.-S. Yoon and B. H. Chung, *J. Phys. Chem. C*, 2010, **114**, 12976-12981.
10 L. Wang, B. Liu, S. Yu, M. Yao, D. Liu, Y. Hou, T. Cui, G. Zou, B. Sundqvist, H. You, D. Zhang and D. Ma, *Chem. Mater.*, 2006, **18**, 4190-4194.
11 M. Yao, B. M. Andersson, P. Stenmark, B. Sundqvist, B. Liu and T. Wågberg, *Carbon*, 2009, **47**, 1181-1188.
12 V. V. Aksenova, R. M. Nikonova, V. I. Lad'yanov and B. E. Pushkarev, *Russ. J. Phys. Chem. A*, 2013, **87**, 1194-1199.
13 C. Park, H. J. Song and H. C. Choi, *Chem. Commun.*, 2009, 4803-4805.
14 R. G. Alargova, S. Deguchi and K. Tsujii, *J. Am. Chem. Soc.*, 2001, **123**, 10460-10467.
15 M. V. Avdeev, A. A. Khokhryakov, T. V. Tropin, G. V. Andrievsky, V. K. Klochkov, L. I. Derevyanchenko, L. Rosta, V. M. Garamus, V. B. Priezzhev, M. V. Korobov and V. L. Aksenov, *Langmuir*, 2004, **20**, 4363-4368.

16 J. A. Brant, J. Labille, J.-Y. Bottero and M. R. Wiesner, *Langmuir*, 2006, **22**, 3878-3885.
17 Q. Ying, J. Marecek and B. Chu, *J. Chem. Phys.*, 1994, **101**, 2665-2672.
18 Q. Ying, J. Marecek and B. Chu, *Chem. Phys. Lett.*, 1994, **219**, 214-218.
19 R. Dattani, K. F. Gibson, S. Few, A. J. Borg, P. A. DiMaggio, J. Nelson, S. G. Kazarian and J. T. Cabral, *J. Colloid Interface Sci.*, 2015, **446**, 24-30.
20 T. Rudalevige, A. H. Francis and R. Zand, *J. Phys. Chem. A*, 1998, **102**, 9797-9802.
21 H. N. Ghosh, A. V. Sapre and J. P. Mittal, *J. Phys. Chem.*, 1996, **100**, 9439-9443.
22 S. Nath, H. Pal and A. V. Sapre, *Chem. Phys. Lett.*, 2003, **369**, 394-401.
23 S. Nath, H. Pal, D. K. Palit, A. V. Sapre and J. P. Mittal, *J. Phys. Chem. B*, 1998, **102**, 10158-10164.
24 A. D. Bokare and A. Patnaik, *J. Phys. Chem. B*, 2005, **109**, 87-92.
25 A. D. Bokare and A. Patnaik, *J. Phys. Chem. B*, 2003, **107**, 6079-6086.
26 X. Yu, W.-B. Zhang, K. Yue, X. Li, H. Liu, Y. Xin, C.-L. Wang, C. Wesdemiotis and S. Z. D. Cheng, *J. Am. Chem. Soc.*, 2012, **134**, 7780-7787.
27 M. V. Avdeev, T. V. Tropin, I. A. Bodnarchuk, S. P. Yaradaikin, L. Rosta, V. L. Aksenov and L. A. Bulavin, *J. Chem. Phys.*, 2010, **132**, 164515.
28 M. V. Avdeev, V. L. Aksenov and T. V. Tropin, *Russ. J. Phys. Chem. A*, 2010, **84**, 1273-1283.
29 A. Mrzel, A. Mertelj, A. Omerzu, M. Čopič and D. Mihailovic, *J. Phys. Chem. B*, 1999, **103**, 11256-11260.
30 S. Nath, H. Pal and A. V. Sapre, *Chem. Phys. Lett.*, 2000, **327**, 143-148.
31 S. Nath, H. Pal and A. V. Sapre, *Chem. Phys. Lett.*, 2002, **360**, 422-428.
32 M. Alfè, B. Apicella, R. Barbella, A. Bruno and A. Ciajolo, *Chem. Phys. Lett.*, 2005, **405**, 193-197.
33 V. Georgakilas, F. Pellarini, M. Prato, D. M. Guldi, M. Melle-Franco and F. Zerbetto, *Proc. Natl. Acad. Sci. U.S.A.*, 2002, **99**, 5075-5080.
34 D. M. Guldi, F. Zerbetto, V. Georgakilas and M. Prato, *Acc. Chem. Res.*, 2005, **38**, 38-43.
35 R. Dattani and J. T. Cabral, *Soft Matter*, 2015, **11**, 3125-3131.
36 H. Hoppe and N. S. Sariciftci, *J. Mater. Chem.*, 2006, **16**, 45-61.
37 C. I. Wang, C. C. Hua and S. A. Chen, *J. Phys. Chem. B*, 2014, **118**, 9964-9973.
38 C. I. Wang and C. C. Hua, *J. Phys. Chem. B*, 2015, **119**, 14496-14504.
39 N. O. McHedlov-Petrossyan, *J. Mol. Liq.*, 2011, **161**, 1-12.
40 X. Zhou, J. Liu, Z. Jin, Z. Gu, Y. Wu and Y. Sun, *Fullerene Sci. Technol.*, 1997, **5**, 285-290.
41 Y. Marcus, A. L. Smith, M. V. Korobov, A. L. Mirakyan, N. V. Avramenko and E. B. Stukalin, *J. Phys. Chem. B*, 2001, **105**, 2499-2506.

42 N. O. McHedlov-Petrossyan, *Chem. Rev.*, 2013, **113**, 5149-5193.

43 C. Y. Yang and A. J. Heeger, *Synth. Met.*, 1996, **83**, 85-88.

44 S. Kwon, J. K. Park, J. Kim, G. Kim, K. Yu, J. Lee, Y.-R. Jo, B.-J. Kim, H. Kang, J. Kim, H. Kim and K. Lee, *J. Mater. Chem. A*, 2015, **3**, 7719-7726.

45 Y. H. Wen, P. C. Lin, C. C. Hua and S. A. Chen, *J. Phys. Chem. B*, 2011, **115**, 14369-14380.

46 A. J. F. Siegert, *MIT Radiation Lab. Report*, 1943, No. 475.

47 S. W. Provenchers, *Comput. Phys. Commun.*, 1982, **27**, 213-227.

48 W. Schärtl, *Light Scattering from Polymer Solutions and Nanoparticle Dispersions*, Springer Verlag, Berlin and Heidelberg, Germany, 2007.

49 M. Doi and S. F. Edwards, *The Theory of Polymer Dynamics*, Oxford Univeristy Press, New York, 1986.

50 I. Teraoka, *Polymer Solutions: An Introduction to Physical Properties*, John Wiley & Sons Ltd., New York, 2002.

51 Z. Meng, S. M. Hashmi and M. Elimelech, *J. Colloid Interface Sci.*, 2013, **392**, 27-33.

52 M. Y. Lin, H. M. Lindsay, D. A. Weitz, R. C. Ball, R. Klein and P. Meakin, *Phys. Rev. A*, 1990, **41**, 2005-2020.

53 A. A. Kaznacheevskaya, O. A. Kizima, L. A. Bulavin, A. V. Tomchuk, V. M. Garamus and M. V. Avdeev, *J. Surf. Invest.: X-ray, Synchrotron Neutron Tech.*, 2013, **7**, 1133-1136.

54 T. M. Stawski, R. Besselink, S. A. Veldhuis, H. L. Castricum, D. H. A. Blank and J. E. ten Elshof, *J. Colloid Interface Sci.*, 2012, **369**, 184-192.

55 M. V. Avdeev, T. V. Tropin, V. L. Aksenov, L. Rosta and M. T. Kholmurodov, *J. Surf. Invest.: X-ray, Synchrotron Neutron Tech.* , 2008, **2**, 819-825.

56 S. J. Henderson, *Langmuir*, 1997, **13**, 6139-6145.

57 S.-H. Chen and J. Teixeira, *Phys. Rev. Lett.*, 1986, **57**, 2583-2586.

58 P. Hiemenz and R. Rajagopalan, *Principles of Colloid and Surface Chemistry*, Marcel Dekker, New York, 3rd edn., 1997.

59 N. R. Tummala, C. Sutton, S. G. Aziz, M. F. Toney, C. Risko and J.-L. Bredas, *Chem. Mater.*, 2015, **27**, 8261-8272.

60 L. Bulavin, I. Adamenko, Y. Prylutskyy, S. Durov, A. Graja, A. Bogucki and P. Scharff, *Phys. Chem. Chem. Phys.*, 2000, **2**, 1627-1629.

61 Y. I. Prylutskyy, A. S. Buchelnikov, D. P. Voronin, V. V. Kostjukov, U. Ritter, J. A. Parkinson and M. P. Evstigneev, *Phys. Chem. Chem. Phys.*, 2013, **15**, 9351-9360.

62 G. V. Andrievsky, V. K. Klochkov, E. L. Karyakina and N. O. McHedlov-Petrossyan, *Chem. Phys. Lett.*, 1999, **300**, 392-396.

63 D. N. LeBard, B. G. Levine, R. DeVane, W. Shinoda and M. L. Klein, *Chem. Phys. Lett.*, 2012, **522**, 38-42.

64 A. A. Thorat and S. V. Dalvi, *CrystEngComm*, 2014, **16**, 11102-11114.
65 S. R. Aragon and R. J. Pecora, *J. Chem. Phys.*, 1976, **64**, 2395.
66 H. Wu, J. Xie, M. Lattuada and M. Morbidelli, *Langmuir*, 2005, **21**, 3291-3295.
67 L. A. Bulavin, I. I. Adamenko, V. M. Yashchuk, T. Y. Ogul'chansky, Y. I. Prylutskyy, S. S. Durov and P. Scharff, *J. Mol. Liq.*, 2001, **93**, 187-191.
68 G. Török, V. T. Lebedev and L. Cser, *Phys. Solid State*, 2002, **44**, 572-573.
69 F. Pignon, A. Magnin, J.-M. Piau, B. Cabane, P. Lindner and O. Diat, *Phys. Rev. E*, 1997, **56**, 3281-3289.
70 I. V. Zolotukhin, L. I. Yanchenko and E. K. Belonogov, *JETP Lett.*, 1998, **67**, 720-722.
71 L. Zheng and Y. Han, *J. Phys. Chem. B*, 2012, **116**, 1598-1604.
72 S. Keiji, I. Naoko and M. Akito, *Jpn. J. Appl. Phys.*, 2015, **54**, 06FK05.
73 A. C. Johnsson, M. C. Camerani and Z. Abbas, *J. Phys. Chem. B*, 2011, **115**, 765-775.
74 L. Nicoleau, T. Gädt, L. Chitu, G. Maier and O. Paris, *Soft Matter*, 2013, **9**, 4864-4874.
75 X. Han, Z. Xiong, X. Zhang and H. Liu, *Soft Matter*, 2015, **11**, 2139-2146.
76 N. E. Kurland, J. Kundu, S. Pal, S. C. Kundu and V. K. Yadavalli, *Soft Matter*, 2012, **8**, 4952-4959.
77 B. J. Berne and R. Pecora, *Dynamic Light Scattering: With Applications to Chemistry, Biology, and Physics* Dover, New York, 2000.
78 A. V. Eletskii, M. V. Okun and B. M. Smirnov, *Phys. Scripta*, 1997, **55**, 363.
79 G. Fytas, H. G. Nothofer, U. Scherf, D. Vlassopoulos and G. Meier, *Macromolecules*, 2002, **35**, 481-488.
80 J. Li, W. Li, H. Huo, S. Luo and C. Wu, *Macromolecules*, 2008, **41**, 901-911.
81 S. Koizumi and T. Inoue, *Soft Matter*, 2011, **7**, 9248-9258.
82 M. Długosz and J. M. Antosiewicz, *J. Chem. Theory Comput.*, 2014, **10**, 481-491.
83 L. Ehrl, M. Soos and M. Lattuada, *J. Phys. Chem. B*, 2009, **113**, 10587-10599.

Table of Content

Mesoscale aggregation properties of C_{60} in toluene and chlorobenzene

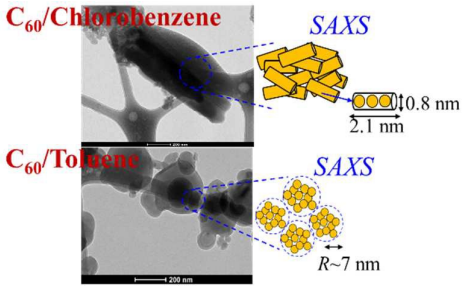

Solvent-induced, nanoscale aggregate units lead to a hierarchy of mesoscale aggregation features as revealed by multiscale experimental schemes.